

Supplementary Information for “Analytical electron microscopy study of the composition of BaHfO₃ nanoparticles in REBCO films: The influence of rare-earth ionic radii and REBCO composition”

L. Grünewald,^{a†} P. Cayado,^{b,c†*} M. Erbe,^b J. Hänisch,^{b*} B. Holzapfel,^b and D. Gerthsen^a

^a Karlsruhe Institute of Technology (KIT), Laboratory for Electron Microscopy (LEM), Karlsruhe, Germany

^b Karlsruhe Institute of Technology (KIT), Institute for Technical Physics (ITEP), Eggenstein-Leopoldshafen, Germany

^c University of Geneva, Department of Quantum Matter Physics (DQMP), Quai Ernest-Ansermet 24, 1211 Geneva, Switzerland

† Authors contributed equally to this work.

* Corresponding author (jens.haenisch@kit.edu, pablo.cayado@unige.ch)

Nanoparticle-Size Analysis

The BaHfO₃ (BHO) nanoparticle sizes were approximated from the measured particle areas obtained from STEM cross-section images (Figure S1). Nanoparticles in LAADF/HAADF-STEM images were manually labeled using the Labkit plugin¹ (<https://imagej.net/plugins/labkit>) for Fiji². Nanoparticles at the substrate interface and the film surface were ignored. Nanoparticles in contact with each other in the segmented binary images were separated by a Watershed algorithm. For 5-REBCO, 186 particles were measured from multiple images. The projected areas A of the segmented nanoparticles were determined by the “Analyze Particles...” function in Fiji. For further particle-size analysis, we used a procedure based on Limpert et al.³. The equivalent diameters d of circles with the equal area A as the measured nanoparticle projections were calculated with $d = \sqrt{4A/\pi}$. A log-normal distribution $f(x) = (2\pi\sigma^2x^2)^{-0.5} \cdot \exp(-(\ln(x) - \mu)^2 / (2\sigma^2))$ with parameters μ and σ was fitted to the normalized histogram. The mode m (i.e. the position of the maximum of the distribution), the arithmetic mean μ_a , and the arithmetic standard deviation σ_a were calculated using $m = \exp(\mu - \sigma^2)$, $\mu_a = \exp(\mu + 0.5\sigma^2)$, and $\sigma_a = \exp(\mu + 0.5\sigma^2) \cdot \sqrt{\exp(\sigma^2) - 1}$, respectively. The errors correspond to the propagated fitting errors (standard deviations) from μ and σ using the “uncertainties” Python package⁴.

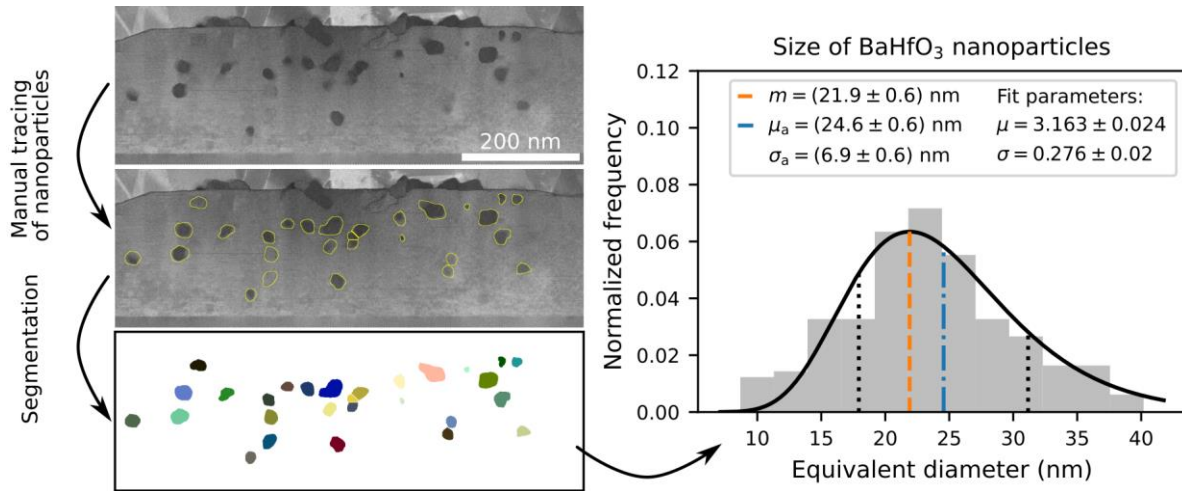


Figure S1. Schematic workflow describing the determination of BaHfO₃-nanoparticle size in REBCO films based on cross-section STEM images. Left: The nanoparticles are manually traced, and their projected areas are measured after segmentation. Right: Plot of the normalized histogram of the calculated equivalent diameters (gray), fitted log-normal distribution (black curve), mode m (dashed orange line), arithmetic mean μ_a (dashed-dotted blue line), and range containing 68.3% of the area under the curve (“1 sigma”, dotted black lines).

BaHfO₃ and RE₂O₃ Nanoparticles at the REBCO-SrTiO₃ Interface

BaHfO₃ nanoparticles and RE₂O₃ precipitates typically grow with epitaxial alignment near the REBCO-SrTiO₃ interface (Figure S2 and Figure S3). For example, the unfiltered HAADF-STEM image in Figure S2a shows a cross-section image near the film-substrate interface for (Gd,Dy,Y,Ho,Er)BCO (5-REBCO) with two particles near the interface. The parallel alignment of the REBCO planes around the magnified stacking fault (inset in Figure S2a) is used to identify the REBCO alignment, here viewed along the [010] zone axis. Noise removal by background-image subtraction followed by average-background-subtraction filtering (Figure S2b, ABSF^{5,6}) and subsequent Fourier-transform analysis (Figure S2c) reveals the different phases and their crystallographic relationships. The magnified region shows the close match of lattice-plane distances for the shown crystallographic orientations leading to epitaxial growth. The separate Fourier transforms of the regions marked by green-, yellow- and pink-dashed lines in Figure S2b are shown in Figure S2d with phases on the basis of the identified crystal structures listed in Table S1.

Table S1: Crystal structures of identified phases shown in Figure S2 taken from the inorganic crystal structure database (ICSD)⁷. YBCO and Y₂O₃ were taken as approximation for (Gd,Dy,Y,Ho,Er)BCO and (Gd,Dy,Y,Ho,Er)₂O₃. BaHfO₃ was created by modifying the lattice parameter for the given BaZrO₃ structure⁸.

Structure	ICSD number	Lattice type	Lattice parameter(s) (Å)
SrTiO ₃	23076	Cubic	3.905
BaHfO ₃	90049 ¹	Cubic	4.171
YBa ₂ Cu ₃ O _{7-δ}	56507	Orthorhombic	$a = 3.8209$ $b = 3.8843$ $c = 11.6767$
Y ₂ O ₃	23811	Cubic	10.604

¹ A BaZrO₃ structure was modified to BaHfO₃ with the lattice parameter taken from ref. ⁸ since a BaHfO₃ file was not available in the ICSD database at the time of writing.

High-resolution HAADF-STEM imaging (Figure S3) reveals that BHO growth starts after one entire unit cell of REBCO along the growth direction (Figure S3a, solid arrow) in accordance with Molina-Luna et al.⁹. In contrast, RE₂O₃ already starts at the first RE plane of the first REBCO unit cell (Figure S3b, dashed arrow). For a better visibility, the images on the right-hand side of Figure S3 depict the denoised images (using AtomSegNet¹⁰) of the ABS-filtered HAADF-STEM images on the left-hand side. The RE₂O₃ growth on top of a cubic perovskite-like REBCO phase (cf. yellow brackets in Figure S3b) on STO is in accordance with Haage et al.¹¹, where the REBCO film initially forms a cubic perovskite phase during nucleation on STO. RE₂O₃ close to the film-substrate interface seemingly grows directly on this initial cubic REBCO phase.

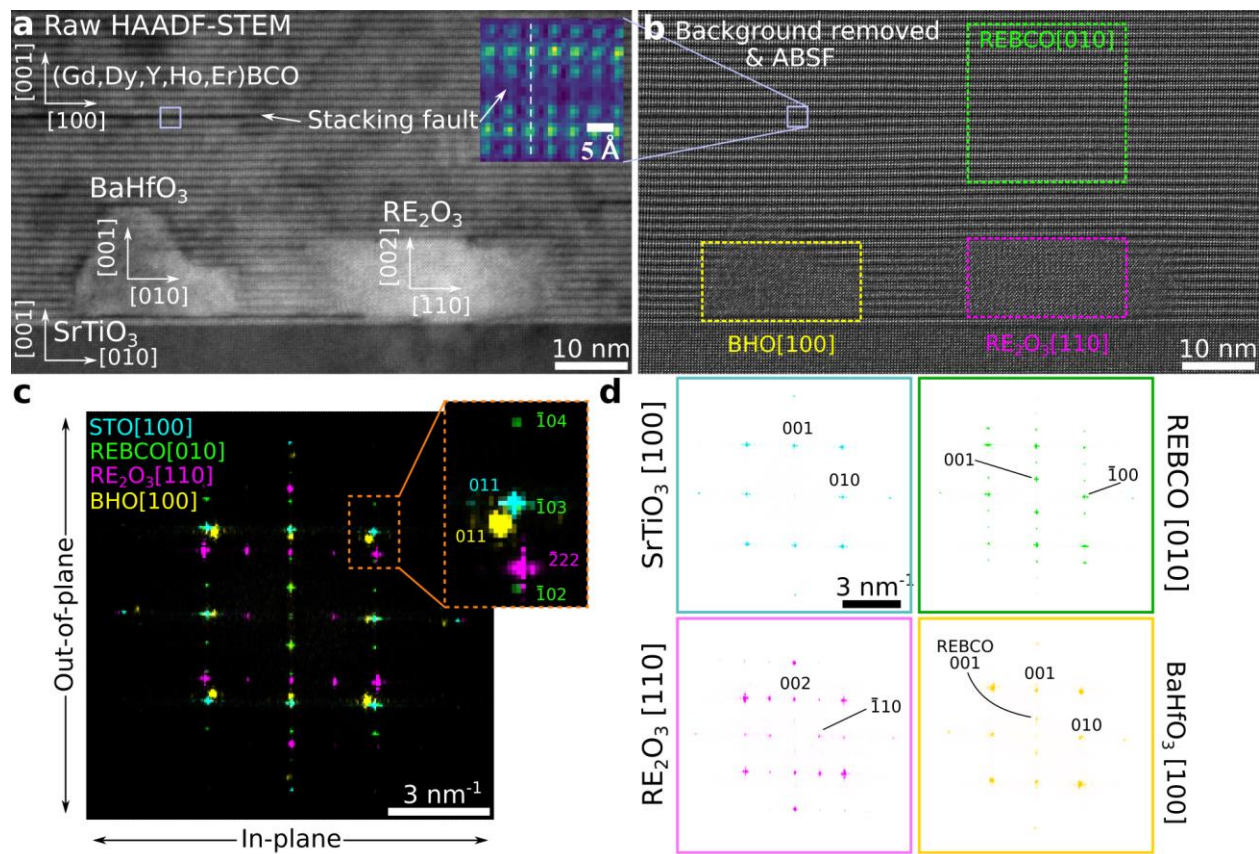


Figure S2. Fourier-transform analysis of the REE-rich precipitate/BHO particle (Figure 3 in the main text). **a** Raw and **b** filtered overview HAADF-STEM images of precipitates near the film-substrate interface. The right (left) precipitate is the REE-rich (BHO) particle. The inset in **(a)** shows the (mirror) symmetry of the REBCO unit cells around the stacking fault, which is used to discriminate between the REBCO [100] and [010] orientations. **c** 2D power spectrum (squared modulus of the Fourier transform) of **(b)**, and **d** separate 2D power spectra extracted from the SrTiO₃ substrate and from the regions marked in **(b)** with identified crystalline phases and orientations.

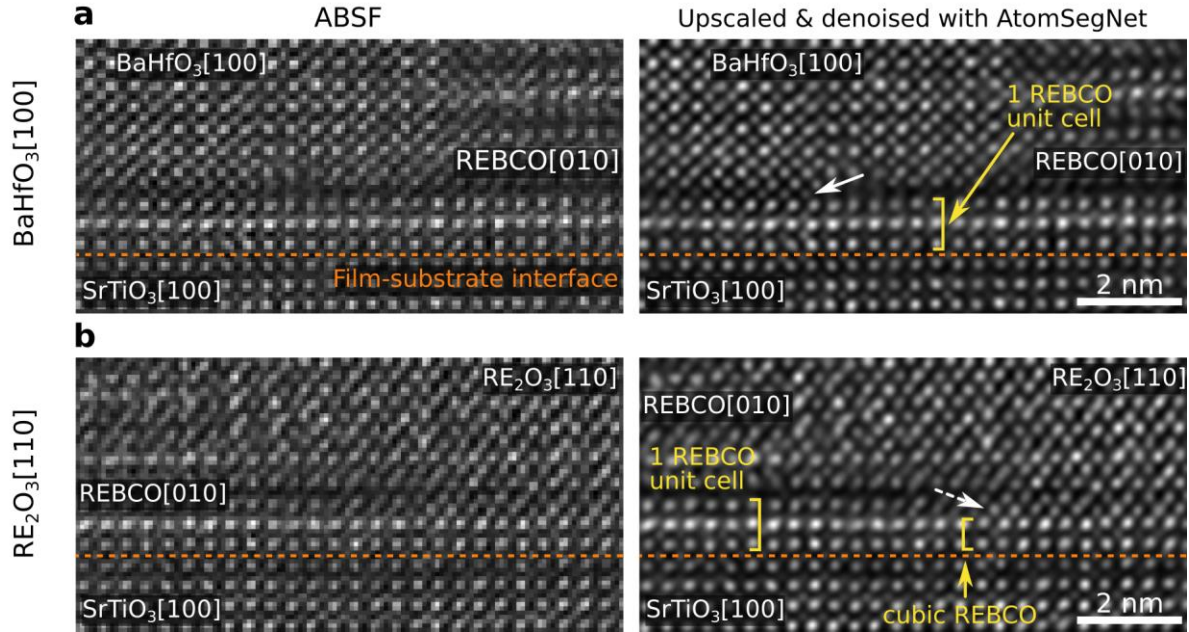


Figure S3. Higher-magnification images of the film-substrate interface (marked by dashed lines) of (a) a BHO[100] and (b) a RE₂O₃[110] precipitate, which are shown in Figure S2. The Miller indices indicate the zone-axis orientations. The images in the right column are four times upscaled and denoised by the “AtomSegNet” convolutional neural network¹⁰ for better visibility. **a** BHO[100] growth near the interface starts at the first CuO plane after one unit cell of REBCO (solid arrow), similar to refs.^{9,12}. **b** RE₂O₃ growth seems to start from the REE plane of the first unit cell of REBCO (dashed arrow).

Validity of STEM-EDXS Analyses

The elemental maps shown in Figure 3 in the main text were extracted from an EDXS dataset that was denoised with principal component analysis (PCA). The latter must be used carefully as it can introduce artifacts into a dataset if, e.g., an insufficient number of principal components is used for reconstruction¹³. The inflection point (“elbow” position) of a scree plot¹⁴ is a commonly used method to determine the necessary number of components to describe most of the variance (i.e. signal without noise) in a dataset. Seven signal components were used in the discussed STEM-EDXS dataset, and the inflection point is clearly visible (Figure S4). We did not observe a change in the elbow position by binning and Gaussian filtering along the spatial dimensions (to increase the signal-to-noise at each pixel) of the STEM-EDXS dataset.

To further rule out possible artifacts by PCA denoising, we also investigated the observed REE-BHO intermixing in the raw, unfiltered EDXS dataset (Figure S5). For this task, binary images were generated for the BHO and REBCO regions, respectively (Figure S5b), and summed-up EDXS spectra were extracted for these regions¹⁵. This results in two EDXS spectra with a high signal-to-noise ratio (Figure S5c,d). The binary masks were determined by thresholding selected elemental maps, e.g., the Hf L α map, for the binary image of the BHO region. Note that the BHO spectrum in Figure S5(d) also contains x-ray signals from the

REBCO region since the nanoparticles (~ 25 nm diameter) are embedded in a thin TEM sample (~ 50 nm thickness) of the REBCO matrix.

A background model taken from the Bruker Esprit software (i.e., power-law-type falling background with specific edges for elements present in the spectrum) and Gaussian functions for each x-ray peak were fitted to the spectra (Figure S5c and d, blue curves). The Gaussian functions have a fixed position (at the known x-ray energy) and width (calculated from the detector's energy resolution). For each element, the whole x-ray line family is fitted since the ratios between different x-ray lines (the so-called line weights) are roughly known from the literature¹⁶. The strongest x-ray line of a family (e.g., $L\alpha$ for the L-line family) is marked by a vertical line. All other x-ray lines of a family are omitted for clarity. The Gaussian peaks for the x-ray lines of each element are shown in the same color.

A good agreement is found between the combined model fit (dark blue line) and the experimental data (red dots), confirming that all relevant elements in the sample and possible spurious x-rays (e.g., $Ni K\alpha$) are included in the model. Note, e.g., the stronger intensity of the Hf $L\alpha$ peak at 7.9 keV for the BHO spectrum (Figure S5d, orange line), which is nearly absent in the REBCO spectrum in Figure S5c.

A *decreasing* trend in REE $L\alpha$ -line intensity is visible for Gd to Er in the REBCO spectrum (Figure S5d). In contrast, an *increasing* trend of REE $L\alpha$ -line intensity is visible from Gd to Er. This trend suggests that REEs with larger atomic number Z (smaller ionic radii) are more strongly incorporated in BHO than REEs with smaller Z . This is the same effect as observed in the PCA-filtered elemental maps shown in Figure 3 in the main text.

Regarding possible peak misidentification, note that the Hf $L\ell$ line at 6.95 keV overlaps with the Er $L\alpha$ line (marked by the orange arrow in Figure S5d). This indicates that the Hf content could influence the Er $L\alpha$ peak height. However, this aspect is included in the model fit where the Hf $L\ell$ line has a fixed ratio to the Hf $L\alpha$ line of $Hf L\ell/Hf L\alpha \sim 0.05$. Therefore, the measured relative increase of the peak height for Er $L\alpha$ in BHO regions compared to REBCO is a real difference in relative concentration in the sample. Note that the $Ni K\alpha$ peak in the spectra results from spurious x-rays generated in the microscope hardware.

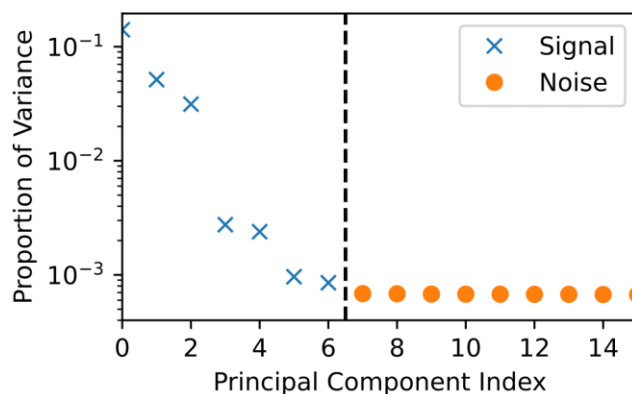


Figure S4. Scree plot after PCA decomposition of the STEM-EDXS dataset. A visible elbow position (marked by the vertical line) identifies seven relevant principal components. The first seven components were used for denoising.

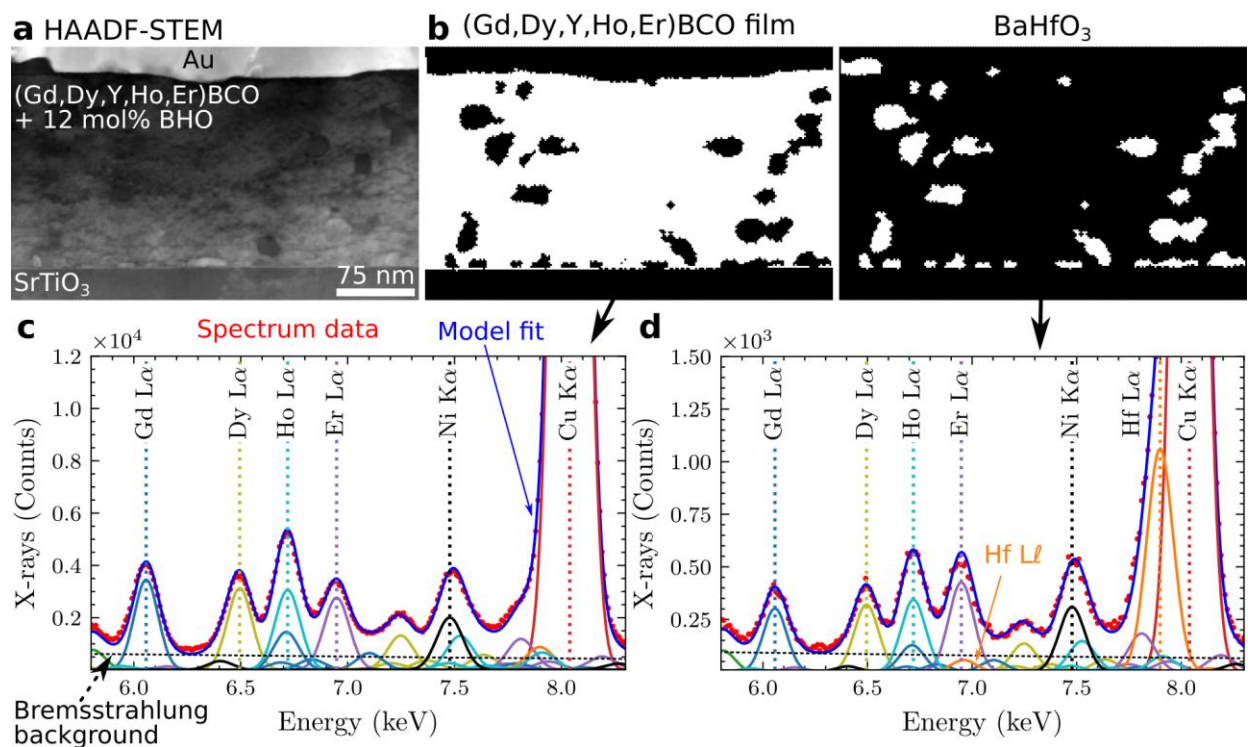


Figure S5. EDXS analysis of summed-up raw spectra from (Gd,Dy,Y,Ho,Er)BCO (5-REBCO) and BHO regions. **a** HAADF-STEM overview image of the STEM-EDXS acquisition region. **b** Binary masks assigned to (Gd,Dy,Y,Ho,Er)BCO (left) and BHO (right) regions. White pixels in the images indicate spectrum image positions which were summed up to the EDXS spectra shown in **(c)** for REBCO and **(d)** BHO. **c** and **d** show the EDXS spectra from REBCO/BHO regions for an energy interval of 5.8 keV to 8.3 keV, including all REE-L α lines and the Hf-L α line. A model fit (blue line) consisting of a background model (dotted black line) and Gaussians for each x-ray line (color-coded by element) was fitted to the data (red dots). Notably, the trend of the REE-L α -peak intensity changes from **(c)** decreasing in REBCO to **(d)** increasing in BHO. This indicates the opposite relative change in composition between REBCO and BHO. The Ni K α peak results from spurious x-rays from the microscope hardware.

Microstructure and Composition of other investigated REBCO Films

Figure S6 presents overview LAADF-STEM cross-section images of (a) (Y,Ho,Er)BCO, (b) SmBCO, (c) GdBCO, and (d) ErBCO films with 12 mol% BHO nanoparticles. The images on the right-hand side present cropped insets from the overview images on the left-hand side (red dashed squares) showing the microstructures at higher magnification. In the latter, stacking faults appear as dark horizontal lines and BHO particles with reduced intensity relative to the REBCO matrix. A few pores are observed for (Y,Ho,Er)BCO, which might stem from the fabrication of TEM-sample preparation.

Low-magnification STEM-EDXS elemental maps for the single-REE REBCO films show a homogeneous distribution of BHO nanoparticles in the films (Figure S7). Notably, a comparably high number density of Er-rich precipitates is visible for ErBCO (cf. arrows in the Er map in Figure S7c), most likely Er_2O_3 . The left region in the elemental maps of ErBCO (marked by a double-headed arrow in the Ba map in Figure S7c) was acquired from a slightly thicker TEM-sample region resulting in a higher x-ray signal in this area. The BHO concentrations were quantified based on STEM-EDXS data and were found to be (11.8 ± 1.6) mol% for SmBCO, (11.8 ± 1.6) mol% for GdBCO, (12.3 ± 1.6) mol% for ErBCO, (12.5 ± 1.5) mol% for 5-REBCO, and (14.1 ± 1.8) mol% for 3-REBCO, i.e., all close to the nominal value of 12 mol% BHO.

Table S2 lists the quantified compositions of masked-sum spectra (for an example, see Figure S5) for all investigated REBCO nanocomposites, i.e. for regions containing only the REBCO matrix or BHO nanoparticles. Note that the elemental concentrations are a convolution of signals of both regions since the nanoparticles are embedded in the REBCO matrix. This results, e.g., in a spurious $\text{Cu } L\alpha$ signal for BHO. The $\text{Cu } L\alpha$ x-ray line was chosen over $\text{Cu } K\alpha$ to reduce the influence of spurious $\text{Cu } K\alpha$ x-rays generated in the used Cu TEM grid. The concentrations are quantified with a standardless Cliff-Lorimer approach¹⁷. To account partly for x-ray absorption of low energy x-rays ($\text{O } K\alpha$ and $\text{Cu } L\alpha$), we assumed an average TEM-sample thickness and density of 75 nm and 7.0 g/cm^3 , respectively. The nominal concentration of $\text{REBa}_2\text{Cu}_3\text{O}_7$ is 7.7 at% RE, 15.4 at% Ba, 23.1 at% Cu, and 53.8 at% O.

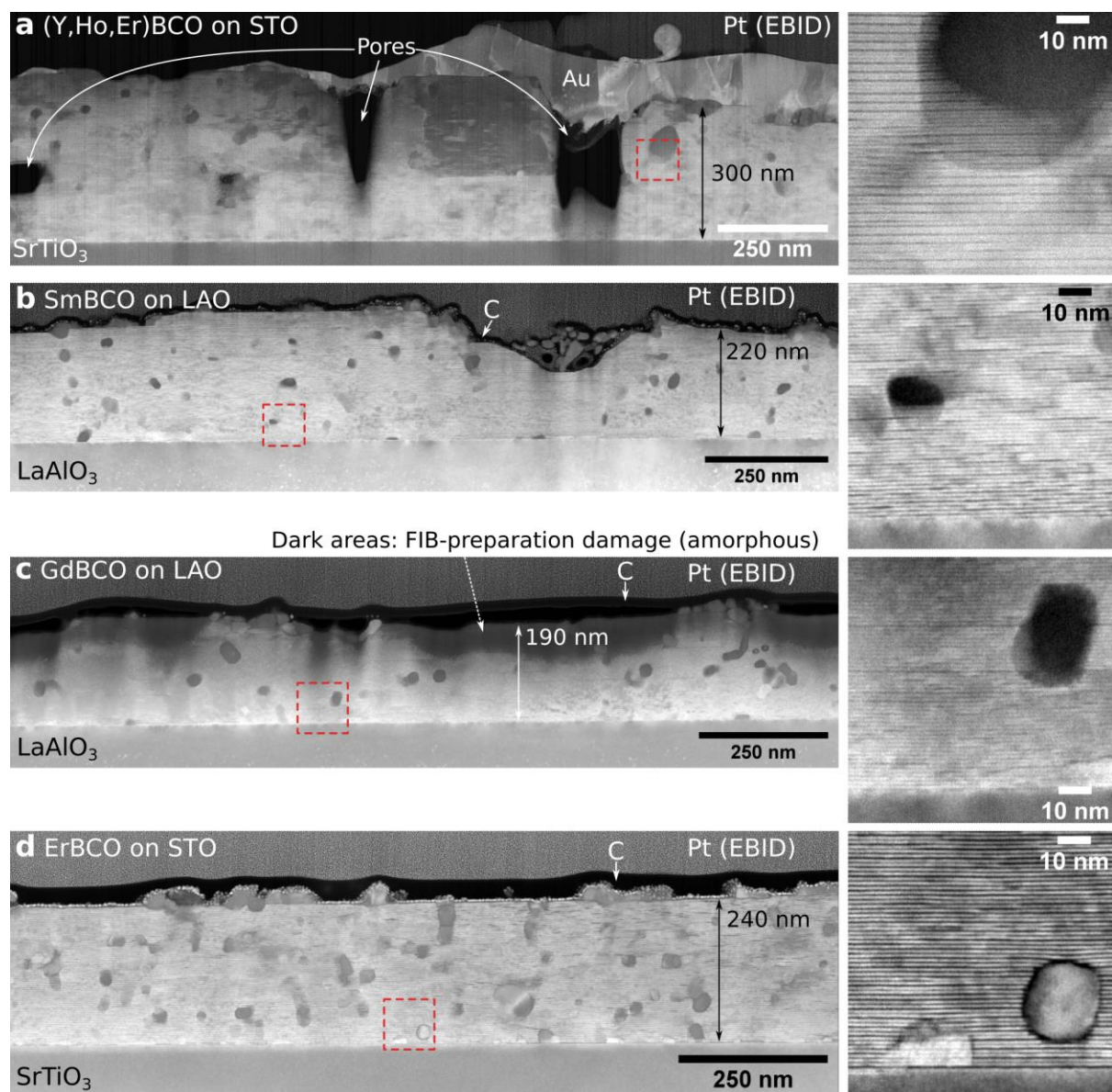


Figure S6. Representative low-angle annular dark-field (LAADF)-STEM overview images (images at the left-hand side) and exemplary $\sim 80 \times 80 \text{ nm}^2$ regions (dashed red squares, images at the right-hand side) of (a) (Y,Ho,Er)BCO, (b) SmBCO, (c) GdBCO, and (d) ErBCO. The film thicknesses vary between $\sim 190 \text{ nm}$ and $\sim 400 \text{ nm}$. Some of the small planar defects visible in the insets in (b) and (c) may be artifacts of TEM-sample preparation by FIB milling or rapid sample degradation during transfer between FIB and TEM instruments. All films are covered by a Pt-protection layer that was deposited by electron-beam-induced deposition (EBID) prior to focused-ion-beam (FIB) TEM-specimen preparation.

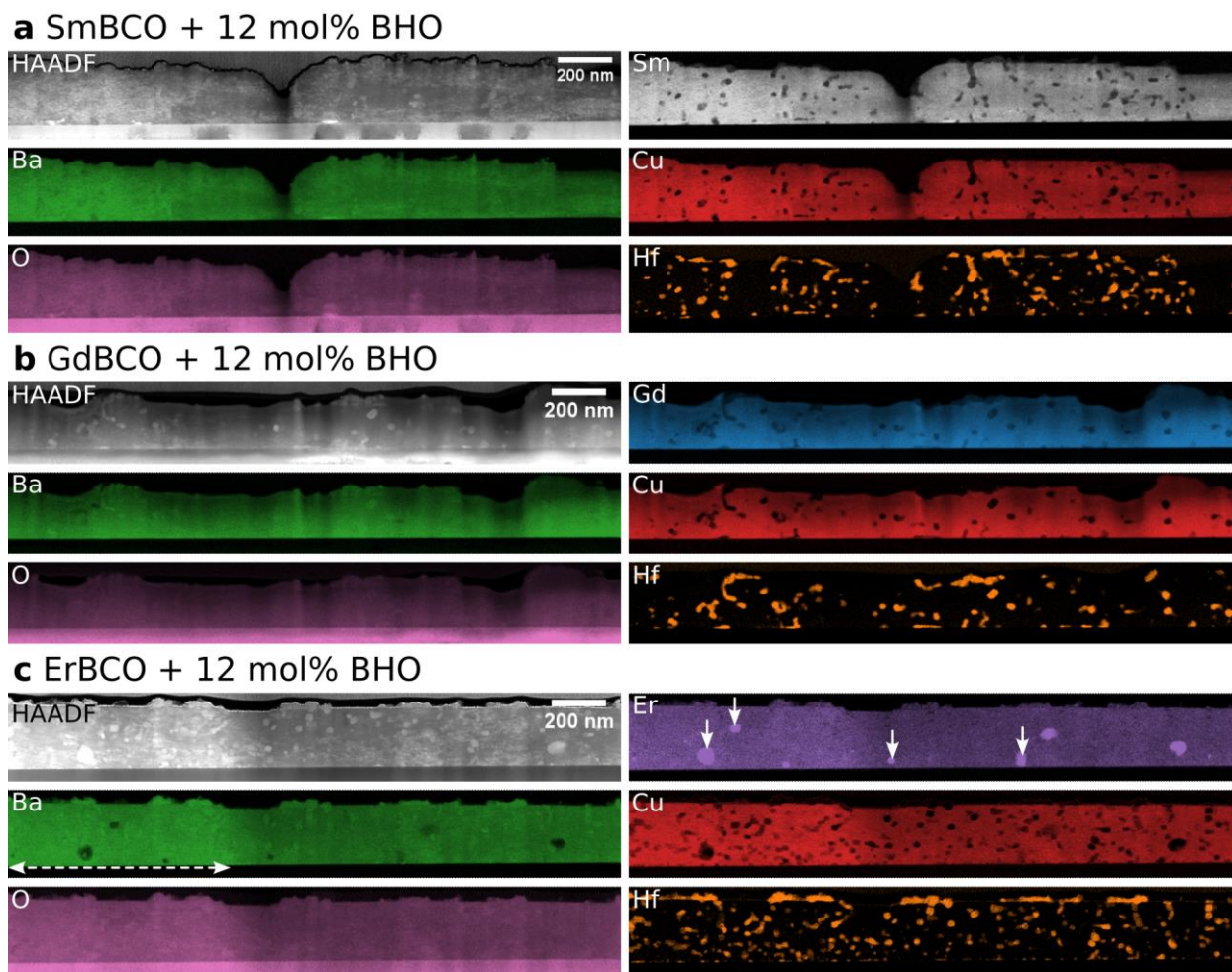


Figure S7. STEM-EDXS elemental maps of (a) SmBCO, (b) GdBCO, and (c) ErBCO. A HAADF-STEM overview image is shown on the top left, together with the corresponding qualitative elemental maps for each sample. A relatively large mapping area ($\sim 2.2 \mu\text{m}$ width) was chosen to sample many BaHfO_3 nanoparticles. The Hf maps visualize the spatial distributions of the latter. **c** The Er map shows local Er enrichment (arrows mark a few examples), probably stemming from Er_2O_3 precipitates. The dashed arrow in the Ba map indicates that the left TEM-sample region was slightly thicker than the right, resulting in higher x-ray signals in the elemental maps.

Table S2: Average elemental concentrations obtained from STEM-EDXS measurements from REBCO matrix and BHO nanoparticle regions. All values are given in at%. The brackets for each element list the x-ray transitions used for quantification.

Sample	Sm (L α)	Gd (L α)	Dy (L α)	Y (K α)	Ho (L α)	Er (L α)	Ba (L α)	Cu (L α)	O (K α)	Hf (L α)
SmBCO matrix	8.2	-	-	-	-	-	12.2	21.8	57.4	0.4
SmBCO BHO	5.4	-	-	-	-	-	11.9	11.7	64.6	6.4
GdBCO matrix	-	7.5	-	-	-	-	11.0	20.2	60.9	0.4
GdBCO BHO	-	5.6	-	-	-	-	11.7	10.1	66.7	5.9
ErBCO matrix	-	-	-	-	-	7.6	12.0	20.3	59.5	0.6
ErBCO BHO	-	-	-	-	-	7.3	13.2	12.0	62.9	4.8
3-REBCO matrix	-	-	-	2.3	2.8	2.6	14.4	22.1	55.0	0.8
3-REBCO BHO	-	-	-	2.0	2.4	2.6	14.8	15.6	58.8	3.8
5-REBCO matrix	-	1.8	1.6	1.2	1.7	1.5	12.9	22.9	55.8	0.7
5-REBCO BHO	-	1.1	1.3	1.1	1.5	1.7	12.7	14.4	61.7	4.6

Oxidation-State Analysis of Rare-Earth Element M-Edges

The local bonding configuration of elements influences the ionic radius. The latter can change the energy loss near edge structure (ELNES) of ionization edges measured by EELS experiments. This aspect was investigated in the SmBCO-, GdBCO-, and ErBCO-BHO nanocomposites for the REE-M edges. Overall, no changes in the REE-M edges ELNES structures were observed between spectra collected on REBCO and BHO areas. This indicates the same valence state (REE^{3+}) in REBCO and BHO. The experimental details are discussed in the following based on Figure S8 and Figure S9.

Figure S8 shows the ELNES analysis of BHO nanoparticles embedded in SmBCO. An overview cross-section ADF-STEM image (Figure S8a) shows the acquisition points of EELS point spectra. The spectra were collected for a few seconds each while summing the EELS signal. For this sample, we choose the point-measurement method over STEM-EELS mapping to mitigate the possibility of spectrometer energy drift during long STEM-EELS-map acquisition.

Point 1 (P1) is taken from the SmBCO matrix and P2 to P5 from BHO nanoparticles. The EELS spectra are (Figure S8b) normalized with the same energy interval (grey shaded area in (b)) for easier comparison. The core-loss edges are marked. The inset shows the comparably weak Hf-M_{4,5} edges, which are only visible for BHO. Besides the Hf edges, the BHO nanoparticles can also be identified by significant Cu depletion (cf. zoom on the Cu-L edges in Figure S8c). The magnified Sm-M edge region is shown in Figure S8d. The Ba-M3 edge causes a small pre-peak in front of the Sm-M₅ edge. Notably, no relative peak shift is visible between the Sm-M_{4,5} white lines for SmBCO (blue) and BHO, as visualized by the vertical lines at ~1082 eV (Sm-M₅ peak) and ~1107 eV (Sm-M₄ peak). The absolute values for the peak positions can be offset from the actual energies due to the possibility of a slight miscalibration of the energy axis (~1-2 eV might be possible). Reference EELS data of Sm by Okayaki et al.¹⁸ shows a ~2-3 eV energy shift of the white lines between Sm³⁺ and Sm²⁺. Since such shifts are not observed here, we conclude that Sm³⁺ does not change its oxidation state in BHO.

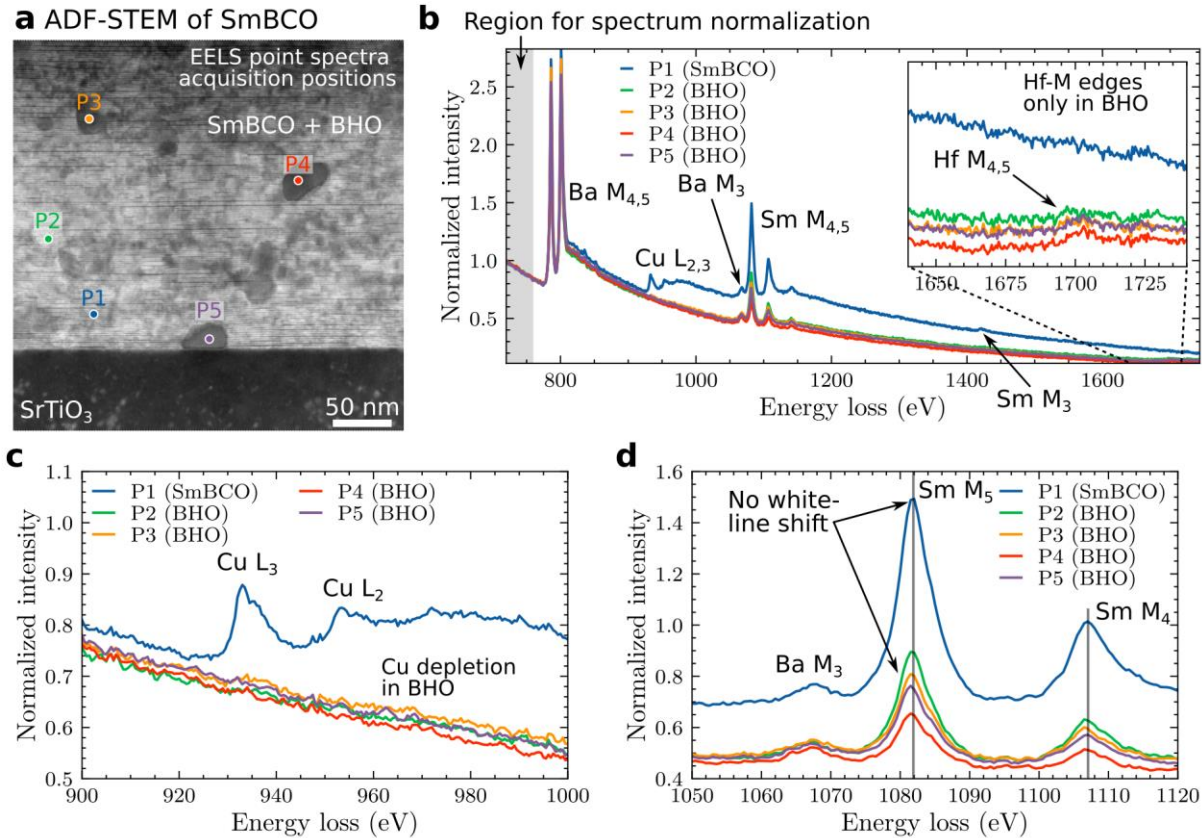


Figure S8. ELNES analysis of BHO nanoparticles embedded in SmBCO. **a** Overview cross-section ADF-STEM image with marked acquisition points of EELS point spectra. **b** EELS spectra were acquired from the positions in **(a)** with the marked core-loss edges (normalized to the integrated intensity in the gray-shaded area for comparison). The inset shows the weak Hf-M_{4,5} edges for BHO. **c** Magnified Cu-L-edge region without Cu signal for BHO particles. **d** Magnified Sm-M-edge region. No relative peak shift is visible between the Sm-M_{4,5} white lines for SmBCO (blue) and BHO spectra, indicating the same valence state Sm³⁺ in REBCO and BHO.

A similar analysis was performed for ErBCO (Figure S9a–c) and on a STEM-EELS map of GdBCO (Figure S9d–f). Starting with ErBCO, a spectrum from an Er-rich precipitate (P1 in Figure S9a) was acquired besides BHO and ErBCO regions. The spectra were normalized to the peak intensity of the Er-M₅ white-line peak and plotted together in Figure S9b. All spectra overlap well, even with a reference spectrum taken from the EELS Atlas by Gatan¹⁹. Similar to SmBCO, no changes in the ELNES are observed for BHO particles in ErBCO, indicating Er³⁺ in REBCO and BHO. Figure S9c shows how the Er-M_{4,5} peak intensities were extracted using a non-linear least square (NLLS) fit in DigitalMicrograph. A Lorentzian function for the comparably weak Er M₄ peak yielded better results and fit stability than a Gaussian. A similar method was used to extract the M_{4,5} peak intensities for SmBCO (not shown) and GdBCO (Figure S9d). The average M₄/M₅ ratios determined from all available measurements were 0.32 ± 0.02 (Sm), 0.44 ± 0.02 (Gd), and 0.10 ± 0.01 (Er), which is comparable to other publications^{20,21}.

The ELNES analysis of GdBCO was done on STEM-EELS mapping datasets (Figure S9d–f). NLLS fitting of Gaussians yields the intensities, positions, and peak widths of the $M_{4,5}$ white lines. The spatial distributions of the Gd- $M_{4,5}$ peak intensities are shown in Figure S9e, together with the calculated M_4/M_5 ratio map. No change in the M_4/M_5 ratio is visible in the BHO region. The change in $M_{4,5}$ peak positions is displayed in Figure S9f. A gradient from left to right is visible in the Gd $M_{4,5}$ positions, which stems from an energy drift of the spectrometer during the acquisition (a few minutes). Notably, a peak shift is visible near the lower BHO region (solid rectangle in Figure S9f) relative to the GdBCO matrix (dashed rectangle). The difference between the average peak-position values in these two rectangle areas is around 0.5 eV. This small shift could be caused by experimental instability. The difference in peak positions M_4 - M_5 is plotted on the right in Figure S9f and shows no remarkable change between GdBCO and BHO, indicating that line shifts are not associated with changes of the valence state.

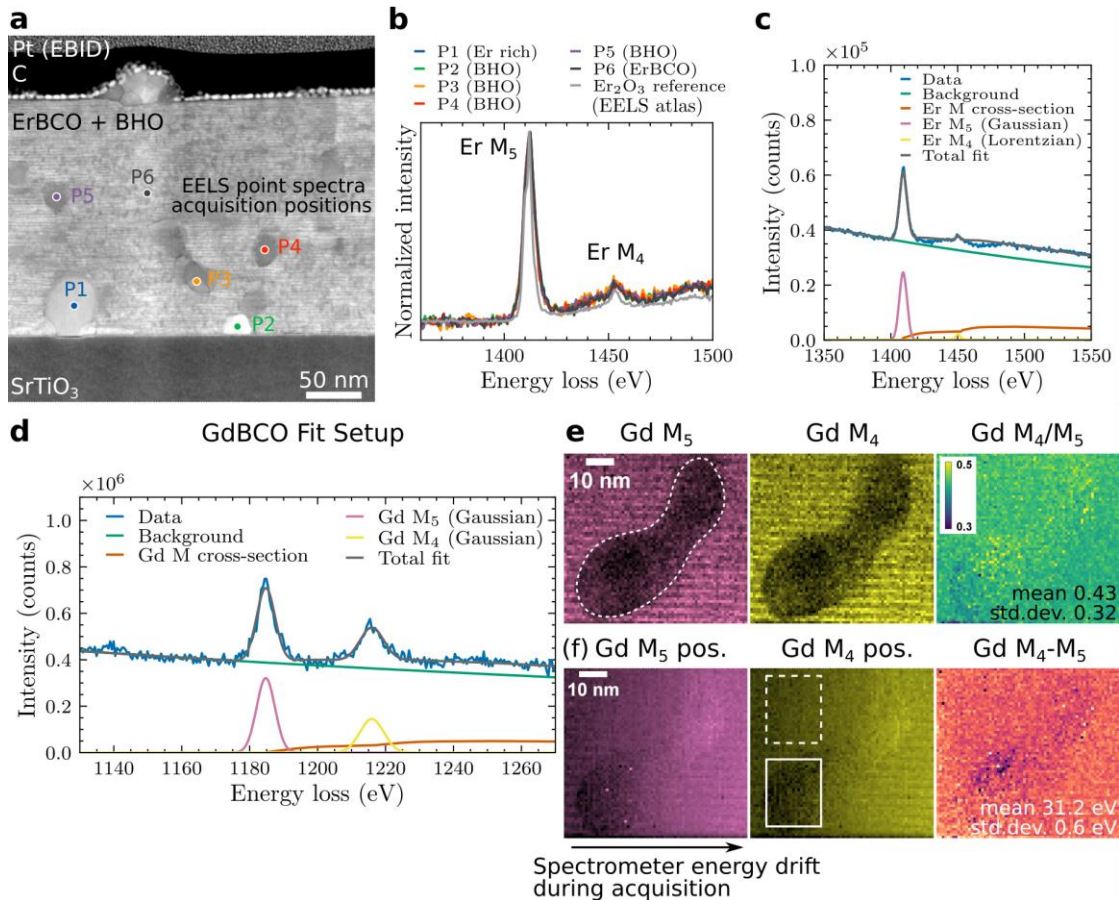


Figure S9. ELNES analysis of the REE- $M_{4,5}$ edges for the REBCO-BHO nanocomposites ErBCO (top, a–c) and GdBCO (bottom, d–f). **a** Overview ADF-STEM image of ErBCO with marked acquisition points. **b** Normalized and overlaid EELS spectra from the positions in (a). (c, d) NLLS-fit setup used to extract the (c) Er- and (d) Gd- $M_{4,5}$ peak intensities, positions, and widths. (e, f) Spatial distribution of the (e) Gd- $M_{4,5}$ peak intensities and (f) peak positions around a BHO nanoparticle (position marked by a dashed outline) in GdBCO. The (e) M_4/M_5 ratio and the (f) M_4 - M_5 difference in peak position show no visible differences in the GdBCO and BHO regions.

Ionic Radii for different Lattice Sites in REBCO and BHO

Table S3: Reference ionic radii R_x for different lattice sites in REBCO and BHO used for calculations.

Material	Site	R_x (pm)
REBCO	Y ³⁺ ,CN8	101.9
REBCO	Ba ²⁺ ,CN10	152
BaXO ₃ (A-site)	Ba ²⁺ ,CN12	161
BaHfO ₃	Hf ⁴⁺ ,CN6	71
BaZrO ₃	Zr ⁴⁺ ,CN6	72
BaSnO ₃	Sn ⁴⁺ ,CN6	69
BaTiO ₃	Ti ⁴⁺ ,CN6	60.5

References

- 1 M. Arzt, J. Deschamps, C. Schmied, T. Pietzsch, D. Schmidt, P. Tomancak, R. Haase and F. Jug, *Frontiers in Computer Science*, 2022, **4**, 777728.
- 2 J. Schindelin, I. Arganda-Carreras, E. Frise, V. Kaynig, M. Longair, T. Pietzsch, S. Preibisch, C. Rueden, S. Saalfeld, B. Schmid, J. Y. Tinevez, D. J. White, V. Hartenstein, K. Eliceiri, P. Tomancak and A. Cardona, *Nature Methods*, 2012, **9**, 676–682.
- 3 E. Limpert, W. A. Stahel and M. Abbt, *BioScience*, 2001, **51**, 341–352.
- 4 E. O. Lebigot, Uncertainties: a Python package for calculations with uncertainties, 2010, <https://pythonhosted.org/uncertainties/>
- 5 R. Kilaas, *Journal of Microscopy*, 1998, **190**, 45–51.
- 6 L. Grünwald, M. Langer, S. Meyer, D. Nerz, J. Hänisch, B. Holzapfel and D. Gerthsen, *Supercond. Sci. Technol.*, 2021, **34**, 035005.
- 7 A. Belkly, M. Helderman, V. L. Karen and P. Ulkch, *Acta Crystallographica Section B: Structural Science*, 2002, **58**, 364–369.
- 8 T. Maekawa, K. Kurosaki and S. Yamanaka, *Journal of Alloys and Compounds*, 2006, **407**, 44–48.
- 9 L. Molina-Luna, M. Duerrschabel, S. Turner, M. Erbe, G. T. Martinez, S. V. Aert, B. Holzapfel and G. V. Tendeloo, *Supercond. Sci. Technol.*, 2015, **28**, 115009.
- 10 R. Lin, R. Zhang, C. Wang, X.-Q. Yang and H. L. Xin, *Scientific Reports*, 2021, **11**, 5386.
- 11 T. Haage, J. Zegenhagen, H.-U. Habermeier and M. Cardona, *Phys. Rev. Lett.*, 1998, **80**, 4225–4228.
- 12 T. Maeda, K. Kaneko, K. Yamada, A. Roy, Y. Sato, R. Teranishi, T. Kato, T. Izumi and Y. Shiohara, *Ultramicroscopy*, 2017, **176**, 151–160.
- 13 P. Potapov and A. Lubk, *Advanced Structural and Chemical Imaging*, 2019, **5**, 4.
- 14 R. B. Cattell, *Multivariate Behavioral Research*, 1966, **1**, 245–276.
- 15 D. E. Newbury and D. S. Bright, *Scanning*, 2006, **27**, 15–22.
- 16 N. Ritchie, *Microscopy and Microanalysis*, 2007, **13**, 160–161.
- 17 G. Cliff and G. W. Lorimer, *Journal of Microscopy*, 1975, **103**, 203–207.
- 18 T. Okazaki, K. Suenaga, Y. Lian, Z. Gu and H. Shinohara, *The Journal of Chemical Physics*, 2000, **113**, 9593–9597.
- 19 Gatan, Er₂O₃ thin film spectrum of Er-M edges, <https://eels.info/atlas/erbium>, (accessed December 28, 2022).
- 20 J. A. Fortner and E. C. Buck, *Appl. Phys. Lett.*, 1996, **68**, 3817–3819.
- 21 E. Kennedy, C. Choi and M. C. Scott, *arXiv:2101.06794 [cond-mat]*.